Materials Horizons

ROYAL SOCIETY OF CHEMISTRY

COMMUNICATION

View Article Online
View Journal | View Issue

Cite this: *Mater. Horiz.*, 2022, 9, 403

Received 16th July 2021,
Accepted 30th September 2021

DOI: 10.1039/d1mh01127h

rsc.li/materials-horizons

Regiospecific *N*-alkyl substitution tunes the molecular packing of high-performance non-fullerene acceptors†

Feng Qi,[a] Leighton O. Jones,[b] Kui Jiang,[c] Sei-Hum Jang,[d] Werner Kaminsky,[e] Jiyeon Oh,[f] Hongna Zhang,[g] Zongwei Cai,[g] Changduk Yang,[f] Kevin L. Kohlstedt,[b] George C. Schatz,[b] Francis R. Lin,[*a] Tobin J. Marks[*b] and Alex K.-Y. Jen[*acdeh]

The rapid development of non-fullerene acceptors (NFAs) with strong near-infrared absorption has led to remarkably enhanced short-circuit current density (J_{sc}) values in organic solar cells (OSCs). NFAs based on the benzotriazole (Bz) fused-ring π-core have great potential in delivering both high J_{sc} and decent open-circuit voltage values due to their strong intramolecular charge transfer with reasonably low energy loss. In this work, we have designed and synthesized a series of Bz-based NFAs, PN6SBO-4F, AN6SBO-4F and EHN6SEH-4F, *via* regiospecific *N*-alkyl engineering based on the high-performance NFA mBzS-4F that was reported previously. The molecular packing of mBzS-4F, AN6SBO-4F, and EHN6SEH-4F single crystals was analyzed using X-ray crystallography in order to provide a comprehensive understanding of the correlation between the molecular structure, the charge-transporting properties, and the solar cell performance. Compared with the typical honeycomb single-crystal structure of Y6 derivatives, these NFAs exhibit distinctly different molecular packing patterns. The strong interactions of terminal indanone groups in mBzS-4F and the *J*-aggregate-like packing in EHN6SEH-4F lead to the formation of ordered 3D networks in single-crystals with channels for efficient charge transport. Consequently, OSCs based on mBzS-4F and EHN6SEH-4F show efficient photon-to-current conversions, achieving the highest power conversion efficiency of 17.48% with a J_{sc} of 28.83 mA cm^{-2}.

New concepts

Non-fullerene acceptors (NFAs) play an important role in the development of highly efficient organic solar cells (OSCs). In particular, benzotriazole (Bz)-based NFAs show great potential for achieving high short-circuit current densities with a reasonably low energy loss due to their strong photoresponse in the near-infrared (NIR) region as well as their favorable molecular packing that allows efficient charge transport. In this work, four Bz-based NFAs, **mBzS-4F**, **PN6SBO-4F**, **AN6SBO-4F** and **EHN6SEH-4F**, are synthesized through molecularly engineered regiospecific *N*-alkyl substitution and their single-crystal structures are systematically characterized for the first time. **AN6SBO-4F** has a long linear *n*-amyl chain on the Bz moiety, leading to non-negligible steric hindrance in its molecular packing. By shortening the *n*-amyl to methyl, **mBzS-4F** shows efficient terminal group interactions and face-to-face π-core interactions. On the other hand, **EHN6SEH-4F**, which is *N*-substituted with 2-ethylhexyl chains, forms a *J*-aggregate-like molecular stacking in the out-of-plane direction. OSCs based on PM6:**mBzS-4F** and PM6:**EHN6SEH-4F** show power conversion efficiency (PCE) values of 17.02% and 17.48%, respectively, which can be attributed to the efficient charge transport through the ordered 3D networks formed from strong intermolecular interactions. This work provides a better understanding of the charge-transporting properties of related NFAs, hence providing a rational design strategy for new solar cell materials *via* crystal engineering.

Introduction

New renewable energy technologies that can lower the demand for fossil fuels have received increasing attention recently.

[a] *Department of Chemistry, City University of Hong Kong, Kowloon, 999077, Hong Kong. E-mail: alexjen@cityu.edu.hk, franclin@cityu.edu.hk*
[b] *Department of Chemistry and the Materials Research Center (MRC), Northwestern University, Evanston, Illinois 60208, USA. E-mail: t-marks@northwestern.edu*
[c] *Department of Materials Science and Engineering, City University of Hong Kong, Kowloon, 999077, Hong Kong*
[d] *Department of Materials Science and Engineering, University of Washington, Seattle, Washington 98195-2120, USA*
[e] *Department of Chemistry, University of Washington, Seattle, Washington 98195-2120, USA*
[f] *Department of Energy Engineering, School of Energy and Chemical Engineering, Perovtronics Research Center, Low Dimensional Carbon Materials Center, Ulsan National Institute of Science and Technology (UNIST), 50 UNIST-gil, Ulju-gun, Ulsan 44919, South Korea*
[g] *State Key Laboratory of Environmental and Biological Analysis, Department of Chemistry, Hong Kong Baptist University, Kowloon, 999077, Hong Kong*
[h] *Hong Kong Institute for Clean Energy, City University of Hong Kong, Kowloon, 999077, Hong Kong*

† Electronic supplementary information (ESI) available. CCDC 2096622–2096624. For ESI and crystallographic data in CIF or other electronic format see DOI: 10.1039/d1mh01127h

Among those that have been actively pursued, organic solar cells (OSCs) offer the attraction of being lightweight, solution-processable and composed of earth-abundant materials, and they are readily manufactured by solution-based printing techniques, making them a very attractive candidate.[1–7] Currently, the power conversion efficiency (PCE) of OSCs over 18% has already been achieved[8,9] due to the vigorous development of non-fullerene acceptors (NFAs), which have an extended absorption to the near-infrared (NIR) region, yielding dramatically enhanced short-circuit current density (J_{sc}) values.[10–16]

Among the NFA classes developed, Y6 and its derivatives have been the most investigated because of the remarkable OSC PCEs achieved *via* their closely stacked crescent-shaped molecular geometries with the electron-withdrawing benzo[2,1,3]thiadiazole (BT), fused into the core of the molecular skeleton.[17] Several studies have been reported to illustrate the high performance of Y6-based OSCs from the perspective of crystal engineering.[18–21] Yip *et al.* studied the relationship between the Y6 crystal structure and the performance of the OSCs, explaining the existence of unique molecular stacking in both single-crystal and films, which benefits the exciton delocalization and results in efficient charge generation.[22] Previously, this laboratory also reported a selenium-substituted Y6 derivative, CH1007, demonstrating strong π-core interactions similar to that of Y6 in their single-crystals, which enhanced the charge transport and the PCE.[23] Furthermore, CH1007 possesses two selenophene units with stronger electron-donating properties in the π-core compared with Y6, which led to red-shifted absorption and an enhanced J_{sc}.

By contrast, compared with the BT unit in Y6, benzotriazole (Bz) is a weaker electron-withdrawing unit, making the π-core slightly more electron-rich than Y6, which should not only further extend the NIR absorption due to stronger intramolecular charge transfer (ICT) but also retain a similar low energy loss to Y6.[24–26] Wu *et al.* reported a Bz-based NFA, Y11, which possesses a narrow bandgap of 1.31 eV that yielded a PCE of 16.54% with a high J_{sc} of 26.74 mA cm^{-2} and a non-radiative recombination energy loss of 0.17 eV.[27] This laboratory also designed and synthesized a Bz-based, Se-substituted fused-ring π-core BzS and two NIR-absorbing NFAs, **mBzS-4F** and **EHBzS-4F**, both with bandgaps below 1.25 eV.[28] The **mBzS-4F**-based devices exhibited a high J_{sc} of 27.72 mA cm^{-2}, leading to a PCE of 17.02% with a reasonably small energy loss of 0.446 eV, demonstrating the potential to simultaneously obtain a high J_{sc} and a low energy loss in OSCs with Bz-based NFAs.

However, the molecular packing of Bz-based NFAs has not been systematically characterized in the context of crystal-engineering strategies. Furthermore, side-chain engineering is also a useful strategy to fine-tune the thin-film morphology.[29–33] Sun *et al.* synthesized a series of Y6 derivatives flanked with branched side-chains, showing that the molecular packing is significantly affected by different alkyl chain lengths.[34] The L8-BO-based OSCs exhibit a high PCE of 18.32%, which can be attributed to the improved charge transport due to the enhanced structural order arising from the engineered side-chains.

Compared with BT-based Y6 derivatives, the Bz-based NFAs have an additional site for *N*-alkyl substitution on the Bz moiety. In this work, the length of the linear *N*-alkyl groups on the Bz moiety is systematically altered with methyl, *n*-propyl, and *n*-amyl groups while the same 2-butyloctyl group was retained as the *N*-alkyl substituent on the pyrrole units (Fig. 1). It is also noteworthy that our previously demonstrated NFA, **EHBzS-4F**, substituted with 2-ethylhexyl on the Bz unit and 2-butyloctyl on the pyrrole units, has good solubility but a

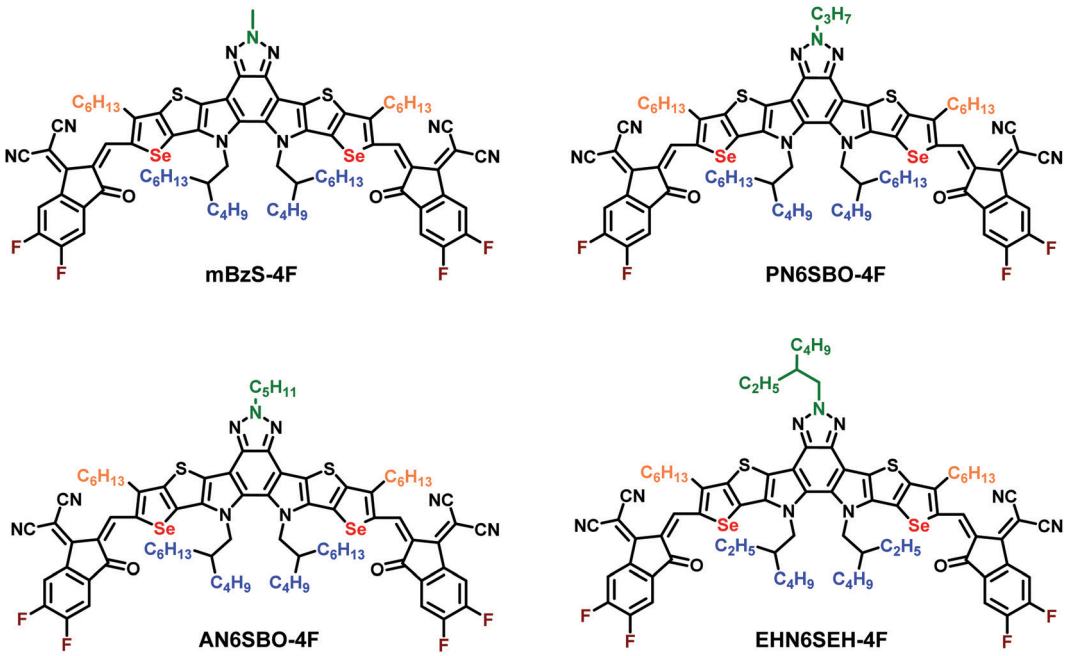

Fig. 1 Molecular structures of the Bz-based NFAs, **mBzS-4F**, **PN6SBO-4F**, **AN6SBO-4F** and **EHN6SEH-4F**.

lower crystallinity.[28] Therefore, the long 2-butyloctyl was replaced with the shorter 2-ethylhexyl group on the pyrrole units, aimed at enhancing the crystallinity while maintaining sufficient solubility for processing. The synthetic routes are shown in Schemes S1 and S2 (ESI†). After different *N*-alkyl-substituted central cores were formylated and condensed with the terminal groups, **PN6SBO-4F**, **AN6SBO-4F** and **EHN6SEH-4F** were yielded. Diffraction-quality single-crystals of **AN6SBO-4F**, **EHN6SEH-4F** and the previously reported **mBzS-4F** were successfully grown to investigate their solid-state structures. The molecular packing of Bz-based NFAs is systematically compared for the first time from the perspective of crystal-engineering strategies.

After carefully analyzing the single-crystal structures, we find distinctly different packing patterns for this series of Bz-based NFAs compared with the typical honeycomb network observed in Y6. **AN6SBO-4F** possesses a longer linear *n*-amyl chain on the Bz moiety which induces more disordered packing and larger distances between neighboring molecules. By shortening the *n*-amyl to methyl, quite efficient terminal-group interactions and face-to-face π-core interactions are created in the **mBzS-4F** unit cell. By contrast, **EHN6SEH-4F** crystallizes with pronounced *J*-aggregate-like packing patterns formed by the π–π stacking between the terminal groups in the out-of-plane direction, leading to a highly ordered 3D network. This suggests that **mBzS-4F** and **EHN6SEH-4F** should be more efficient for charge transport. OSCs based on PM6:**mBzS-4F** deliver a PCE of 17.02% with a J_{sc} of 27.72 mA cm^{-2} and an fill factor (FF) of 76.35%, while that of PM6:**EHN6SEH-4F** also exhibits a high J_{sc} of 28.83 mA cm^{-2} and an FF of 74.64%, resulting in a PCE of 17.48% in accordance with the analysis.

Results and discussion

Fig. 2a and b show the solution and thin-film UV-Vis absorption spectra of the present NFAs, and their optical properties are summarized in Table S1 (ESI†). In a dilute solution of $CHCl_3$, all four acceptors show similar absorption profiles with a maximum peak at ~770 nm. In thin films, the main absorption peaks of **mBzS-4F**, **PN6SBO-4F**, **AN6SBO-4F** and **EHN6SEH-4F** have a characteristic red-shift of ~100 nm. Moreover, **mBzS-4F** has a stronger absorbance than the others in the high photon energy range, showing two distinct 0–1 and 0–2 transition peaks that imply a more ordered microstructure.[35] The optical bandgaps were calculated *via* the absorption onset obtained from the thin-films, and are 1.25, 1.28, 1.27 and 1.29 eV for **mBzS-4F**, **PN6SBO-4F**, **AN6SBO-4F** and **EHN6SEH-4F**, respectively. Such low NFA bandgaps can be a benefit in enhancing the J_{sc}.

The electrochemical properties of the NFAs were measured using cyclic voltammetry. The highest occupied molecular orbital (HOMO) and the lowest unoccupied molecular orbital (LUMO) levels were derived from the onset of the oxidation and reduction potentials (Fig. S1, ESI†). As shown in Fig. 2c, the HOMO/LUMO energy levels of **mBzS-4F**, **PN6SBO-4F**, **AN6SBO-4F** and **EHN6SEH-4F** were calculated to be −5.61/−3.92, −5.63/−3.87, −5.60/−3.88 and −5.59/−3.89 eV, respectively.

Molecular packing has a great influence on OSC charge-transporting properties.[36–38] Therefore, a single-crystal X-ray diffraction study was performed to provide comprehensive insight into the molecular self-assembly in the solid state. Diffraction-quality single-crystals of **mBzS-4F**, **AN6SBO-4F**, and **EHN6SEH-4F** were grown by slow diffusion in a ternary solvent system, and the diffraction data were collected at −173 °C using a single-crystal X-ray diffractometer with Mo-radiation (Tables S2–S4, ESI†). The single-crystal structures are shown in Fig. 3 and the crystal parameters are summarized in Table 1. Besides, the ORTEP view of all single-crystal structures is shown in Fig. S2 (ESI†). All three NFAs show an intramolecular Se–O distance shorter than 2.70 Å (Fig. 3a–c), suggesting an efficient intramolecular non-covalent interaction that helps to form conformational locks between the π-core and terminal groups.[39,40]

Due to the twisted π-core and the special crescent-shaped molecular geometry, enantiomers are formed in the present crystals. Thus, **mBzS-4F** displays as a complicated enantiomeric mixture, having three pairs of *M*/*P*, *M*′/*P*′, and *M*″/*P*″ enantiomers with π-core torsion angles of 13.8(8)°, 11.9(8)° and 16.6(5)°, respectively (Fig. 3d). This special packing may be caused by the comparatively large twist of the π-core. In addition, coplanarity was also computed between the π-core and flanking terminal groups. The D–A dihedral angles of **mBzS-4F** are 3.3(5)°/3.5(9)°,

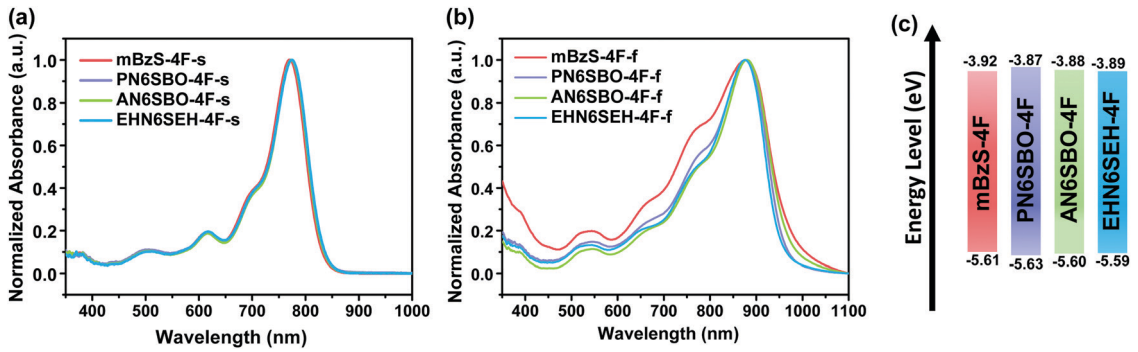

Fig. 2 Normalized UV–vis absorption spectra of **mBzS-4F**, **PN6SBO-4F**, **AN6SBO-4F** and **EHN6SEH-4F** measured as (a) dilute solutions in $CHCl_3$ and (b) thin-films. (c) Frontier orbital energy levels of **mBzS-4F**, **PN6SBO-4F**, **AN6SBO-4F** and **EHN6SEH-4F**.

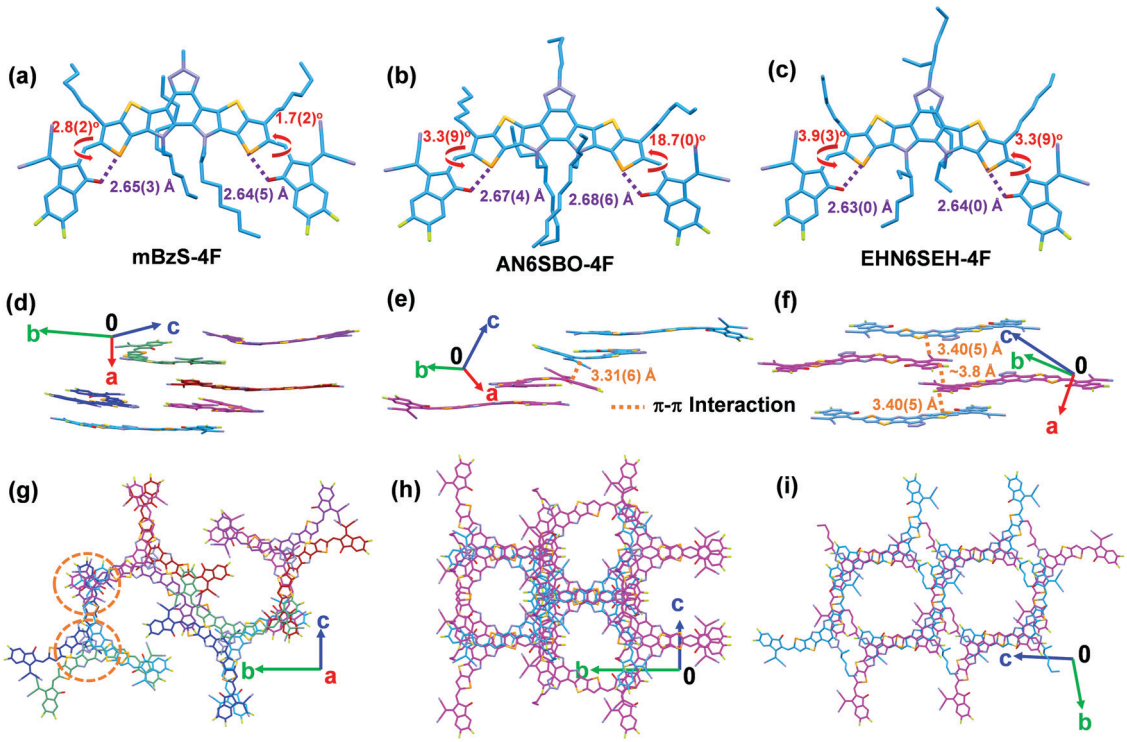

Fig. 3 Single-crystal structures of (a) **mBzS-4F**, (b) **AN6SBO-4F** and (c) **EHN6SEH-4F**. Side view of the molecular packing of (d) **mBzS-4F**, (e) **AN6SBO-4F** and (f) **EHN6SEH-4F**. Top view of the molecular packing of (g) **mBzS-4F**, (h) **AN6SBO-4F** and (i) **EHN6SEH-4F**.

Table 1 Summary of single-crystal parameters of **mBzS-4F**, **AN6SBO-4F** and **EHN6SEH-4F**

NFAs	Chirality	Color	π-Core torsion[a]	D–A dihedral angle[b]	Se–O distance	π–π distance[c]
mBzS-4F	*M*	Azure	13.8(8)°	3.3(5)°/3.5(9)°	2.56(8) Å/2.67(9) Å	—
	P	Pink				
	M′	Blue	11.9(8)°	1.1(0)°/2.9(9)°	2.62(6) Å/2.69(0) Å	
	P′	Brick red				
	M″	Green	16.6(5)°	1.7(2)°/2.8(2)°	2.64(5) Å/2.65(3) Å	
	P′	Purple				
AN6SBO-4F	*M*	Azure	4.2(2)°	3.3(9)°/18.7(0)°	2.67(4) Å/2.68(6) Å	3.31(6) Å
	P	Pink				
EHN6SEH-4F	*M*	Azure	8.6(7)°	3.3(9)°/3.9(3)°	2.63(0) Å/2.64(0) Å	3.40(5) Å
	P	Pink				

[a] The π-core torsion was measured by the two planes determined by the selenophene on different sides of the core. [b] The D–A dihedral angle was obtained *via* the two planes built from the adjacent selenophene and the five-membered ring on indanone. [c] The π–π distance was calculated based on the two planes of the five-membered ring of indanone or selenophene on adjacent NFAs.

1.1(0)°/2.9(9)° and 1.7(2)°/2.8(2)° for the *M*/*P*, *M′*/*P′*, and *M″*/*P″* enantiomers, respectively. **EHN6SEH-4F** possesses a pair of *M*/*P* enantiomers, with a π-core torsion of 8.6(7)° and D–A dihedral angles of 3.3(9)°/3.9(3)° (Fig. 3e). Compared to **mBzS-4F** and **EHN6SEH-4F**, **AN6SBO-4F** also has a pair of *M*/*P* enantiomers corresponding to a π-core torsion of 4.2(2)° and D–A dihedral angles of 3.3(9)°/18.7(0)° (Fig. 3f). We also measured the π–π distances between the closely packed molecules. In **EHN6SEH-4F**, a π–π distance of 3.40(5) Å was measured between two parallel planes defined by the selenophene moieties on adjacent molecules. In **AN6SBO-4F**, the π–π distance was measured between two planes of the five-membered ring of the indanone moiety as 3.31(6) Å. All enantiomers of **mBzS-4F** have a substantial π-core torsion, where a set of parallel planes for determining the π–π distance is not found. Furthermore, π-core interactions can be observed in **mBzS-4F** and **AN6SBO-4F** (Fig. S3, ESI†). This type of π–π stacking of the Bz units has been reported before in the literature.[41] The π-core interaction distances in **mBzS-4F** are 3.44(4) and 3.56(4) Å, which are larger than that (3.19(6) Å) of **AN6SBO-4F**. This can be attributed to the larger π-core torsion of **mBzS-4F**.

In the literature,[19,23] Y6 has an ordered molecular packing that is enabled by two distinct terminal group interactions and a unique face-to-face π-core interaction between the BT unit and the S···N interaction in the adjacent molecules, eventually forming a honeycomb-shaped 3D network. However, **mBzS-4F**,

AN6SBO-4F and **EHN6SEH-4F** show different packing patterns. Top views of the molecular packing of **mBzS-4F**, **AN6SBO-4F** and **EHN6SEH-4F** are shown in Fig. 3g–i. The *N*-alkyl groups on the Bz moiety were not omitted to show their influence on the molecular packing. It was found that longer *N*-alkyl groups on the Bz moiety push away the adjacent molecules and weaken the face-to-face π-core interaction between the head-to-head Bz moieties. The specific long-range order of the crystals is shown in Fig. S4 (ESI†). Note that all crystals have a molecular packing in an oblique direction across the crystal lattice. Although **mBzS-4F** has some disorder in the molecular packing, it still maintains efficient terminal group interactions and face-to-face π-core interactions owing to its shortest *N*-methyl group. However, the linear and longer *n*-amyl group in **AN6SBO-4F** interferes with the molecular packing, leading to disordered packing in the out-of-plane direction, which may undermine the charge transport.

Compared with **mBzS-4F** and **AN6SBO-4F**, the π-core interaction is not well developed in **EHN6SEH-4F** due to the long and branched *N*-alkyl group on the Bz moiety. However, it exhibits *J*-aggregate-like packing patterns between the terminal groups in adjacent molecules, which correlate with the reduced length of the *N*-alkyl group on the pyrrole unit and the reduced steric hindrance compared with **mBzS-4F** and **EHN6SEH-4F**, promoting the formation of a 3D network. This can promote exciton diffusion and improve charge-carrier generation,[42,43] thereby enhancing the J_{sc} value.

To further investigate the intermolecular interactions in the NFAs, grazing-incidence wide-angle X-ray scattering (GIWAXS) analysis was performed. The 2D GIWAXS patterns and the extracted 1D profiles are shown in Fig. S5 (ESI†). All the NFAs show preferred face-on orientations with a clear π–π diffraction peak in the out-of-plane (OOP) direction at ~1.7 $Å^{-1}$ and a lamellar (100) peak at ~0.4 $Å^{-1}$ in the in-plane (IP) direction (Table S5, ESI†). This indicates that all NFAs studied have pronounced π–π stacking, which is beneficial for charge transport. Additionally, the space-charge-limited-current (SCLC) electron mobility measurement was also performed (Fig. S6, ESI†). The electron mobility of **EHN6SEH-4F** is 1.4×10^{-4} $cm^2\ V^{-1}\ s^{-1}$, which is higher than that (9.2×10^{-5} and 8.0×10^{-5} $cm^2\ V^{-1}\ s^{-1}$) of **PN6SBO-4F** and **AN6SBO-4F**, respectively (Table S6, ESI†). **mBzS-4F** also has a high electron mobility of 2.8×10^{-4} $cm^2\ V^{-1}\ s^{-1}$. These results are consistent with the observed molecular packing.

The intermolecular electronic coupling was also computed to provide a better understanding of the charge-transporting properties of these NFAs. First, a reference molecule was chosen in the single crystal and labeled as A, then its close neighbors were labeled as B, C, ⋯, *etc.* (Fig. 4a). **mBzS-4F** has 7 neighboring molecules around the reference, which is more than that (4) of **AN6SBO-4F**. The longer *n*-amyl on the Bz unit and the more twisted D–A dihedral angles of **AN6SBO-4F** reduce the overall coplanarity of the molecule, leading to a less ordered single-crystal packing, and thus fewer intermolecular contacts. By contrast, **EHN6SEH-4F** has 9 neighbors around the reference due to its special packing mode in the oblique direction, leading to an extended intermolecular network. The electronic coupling was calculated using density functional theory (DFT) according to the reported method.[44,45] Fig. 4b shows the couplings of the three acceptors and the detailed values are summarized in Tables S7–S9 (ESI†). It is found that **mBzS-4F**

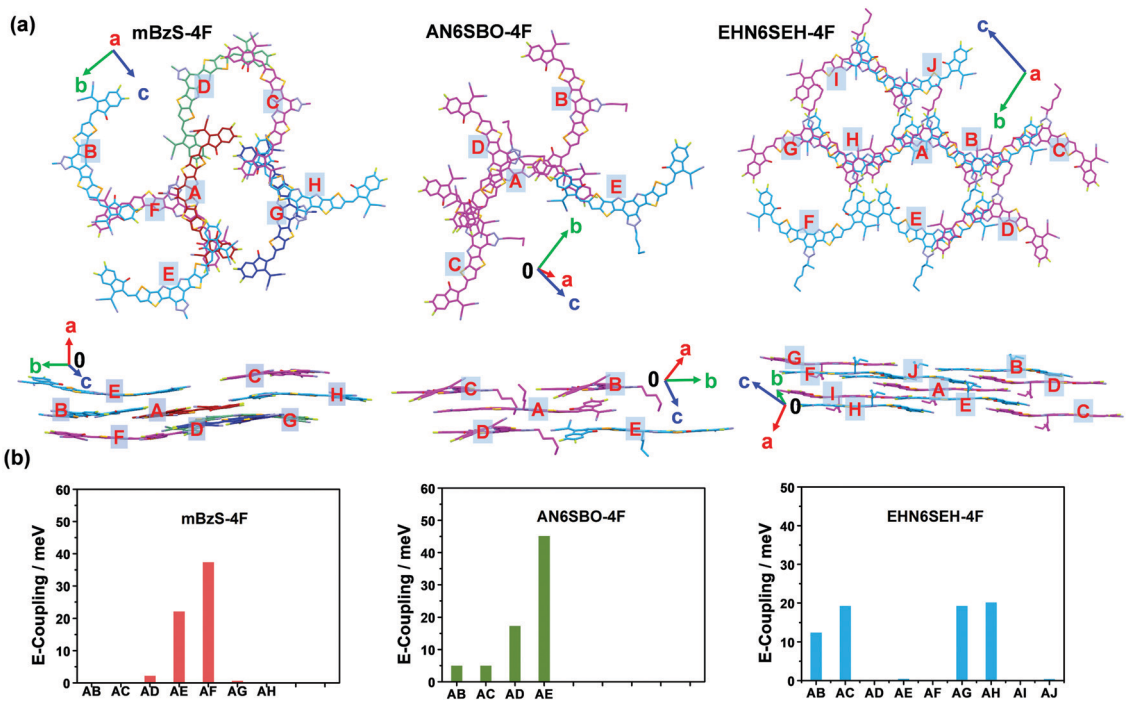

Fig. 4 (a) Top view and side view of the labeled nearest-neighbor molecules in the single-crystal structures of **mBzS-4F**, **AN6SBO-4F** and **EHN6SEH-4F**. (b) Electronic coupling between the nearest neighbors.

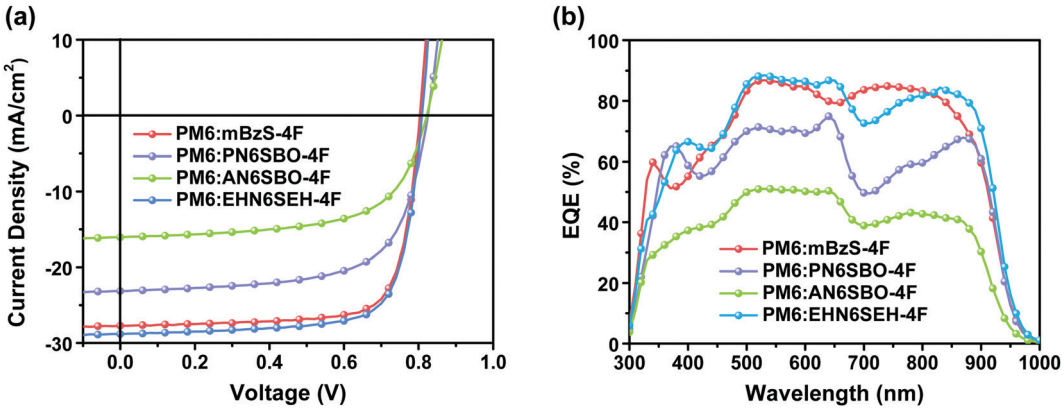

Fig. 5 (a) Solar cell J–V characteristics. (b) EQE curves of the indicated devices based on PM6:**mBzS-4F**, PM6:**PN6SBO-4F**, PM6:**AN6SBO-4F** and PM6:**EHN6SEH-4F**.

has two large couplings, $|J|_{AE}$ = 22.2 meV and $|J|_{AF}$ = 37.4 meV, due to the efficient interactions between terminal groups and π-cores. In comparison, large couplings of $|J|_{AD}$ = 17.4 meV and $|J|_{AE}$ = 45.2 meV were also found in **AN6SBO-4F**, resulting from the *J*-aggregate-like packing of dimers. The four large couplings of $|J|$ = (12.5 (AB), 19.3 (AC), 19.3 (AG), and 20.3 (AH) meV) in **EHN6SEH-4F** show that the reference molecule possesses strong interactions with adjacent molecules, and further forms a long-range channel through the extension of ordered π–π stacking in the single-crystal. A stronger degree of overlapping between adjacent molecules not only leads to a higher degree of electronic coupling but also significantly aids the dissociation of photo-generated excitons and the generation of free charge carriers.[22,46] Furthermore, long-range order in NFA packing enhances the charge transport resulting in a more efficient photon-to-current conversion.

The photovoltaic performance of the PM6:NFA-based OSCs was investigated by fabricating conventional OSCs with an architecture of ITO/PEDOT:PSS/PM6:NFAs/PNDIT-F3N/Ag. The current density–voltage (J–V) plots are shown in Fig. 5a and the performance parameters are summarized in Table 2. The PM6:**mBzS-4F**- and PM6:**EHN6SEH-4F**-based OSCs all exhibit high J_{sc} values of 27.72 and 28.83 mA cm^{-2}, respectively, with a similar open-circuit voltage (V_{oc}) of ∼0.80 V for both, resulting in high PCEs of 17.02% and 17.48%. Meanwhile, these devices also showed higher FF of 76.35% and 74.64%. This may result from the ordered molecular packing that leads to efficient charge transport. By contrast, the devices based on PM6:**PN6SBO-4F** deliver a PCE of only 12.73% with a V_{oc} of 0.825 V, a J_{sc} of 23.13 mA cm^{-2}, and an FF of 66.65%. In addition, the PM6:**AN6SBO-4F**-based devices exhibit a V_{oc} of 0.822 V, a J_{sc} of 16.06 mA cm^{-2}, an FF of 62.98%, and a low PCE of 8.32%. Compared with the Y6-based OSCs, all the devices show slightly lower V_{oc} values, which can be attributed to the reduced NFA bandgap according to the energy gap law.[47] The poor J_{sc} and FF values can be attributed to the lack of a long-range channel with ordered π–π stacking as observed in the crystal structure of **AN6SBO-4F**. To further investigate the relationship between the blend morphology and the photovoltaic performance, atomic force microscopy (AFM) was employed. The mean-square surface roughness (R_q) of PM6:**mBzS-4F**, PM6:**PN6SBO-4F**, PM6:**AN6SBO-4F**, and PM6:**EHN6SEH-4F** blend films are 0.93, 3.09, 2.86 and 0.86 nm, respectively (Fig. S7, ESI†). The rougher surface in the PM6:**PN6SBO-4F** and PM6:**ANSBO-4F** films may lead to unfavorable charge-transport properties and serious recombination, resulting in lower J_{sc} and FF values.[48–50]

To further investigate the photoresponse of devices based on PM6:NFAs, external quantum efficiency (EQE) spectra were collected (Fig. 5b). The PM6:**mBzS-4F**-based devices show efficient charge generation in the region of 465–875 nm with EQEs over 70%. The devices based on PM6:**EHN6SEH-4F** also exhibit a broad photoresponse from 460 to 900 nm with an EQE value above 70%. However, the PM6:**PN6SBO-4F**- and PM6:**AN6SBO-4F**-based devices display relatively weak photoresponses. This may be due to the disordered molecular packing caused by their long *N*-alkyl groups on the Bz moiety. Note that the integrated photocurrent densities of the PM6:**mBzS-4F**-, PM6:**PN6SBO-4F**-, PM6:**AN6SBO-4F**-, and PM6:**EHBzS-4F**-based devices are 27.17, 22.21, 15.20 and 27.80 mA cm^{-2}, respectively, which agree well with J_{sc} extracted from the J–V plots.

Table 2 Photovoltaic parameters of the optimized devices based on PM6:**mBzS-4F**, PM6:**PN6SBO-4F**, PM6:**AN6SBO-4F** and PM6:**EHN6SEH-4F** blends

Blends	V_{oc} (V)	J_{sc} (mA cm^{-2})	Integrated J_{sc} (mA cm^{-2})	FF (%)	PCE (%)
PM6:**mBzS-4F**	0.804	27.72	27.17	76.35	17.02
PM6:**PN6SBO-4F**	0.825	23.13	22.21	66.65	12.73
PM6:**AN6SBO-4F**	0.822	16.06	15.20	62.98	8.32
PM6:**EHN6SEH-4F**	0.809	28.83	27.80	74.64	17.48

Conclusions

We have designed and synthesized a series of NIR-absorbing Bz-based NFAs, **mBzS-4F**, **PN6SBO-4F**, **AN6SBO-4F** and **EHN6SEH-4F**, by introducing various linear *N*-alkyl groups (methyl, *n*-propyl, and *n*-amyl) and branched *N*-alkyl groups

(2-ethylhexyl and 2-butyloctyl) onto the Bz and pyrrole moieties on the NFA π-cores. All NFAs show a bandgap below 1.30 eV, resulting from the enhanced ICT due to a more electron-rich central π-core than that of Y6. For the first time, diffraction-quality single-crystals of Bz-based NFAs were grown and systematically investigated to study the influence of different *N*-alkyl groups on the solid-state intermolecular interactions. Efficient terminal-group interactions and face-to-face π-core interactions are maintained in **mBzS-4F**, which possesses the shortest *N*-methyl alkyl group on the Bz moiety. Although the π-core interaction in **EHN6SEH-4F** has completely disappeared due to its longer *N*-alkyl group on the Bz moiety, it still forms efficient charge-transport channels induced by the strong intermolecular interactions of terminal groups between adjacent molecules. This enables *J*-aggregate-like stacking and a 3D network. However, the longer linear *n*-amyl on the Bz moiety of **AN6SBO-4F** results in poor long-range order in the molecular packing, which undermines the charge transport. Consequently, the PM6:**mBzS-4F**- and PM6:**EHN6-SEH-4F**-based OSCs exhibit high J_{sc} values of 27.72 and 28.83 mA cm^{-2}, respectively, resulting in high PCEs of 17.02% and 17.48%, respectively. By contrast, the devices based on PM6:**PN6SBO-4F** and PM6:**AN6SBO-4F** only deliver PCEs of 12.73% and 8.32%, respectively. This work provides a better understanding of the charge-transporting properties of related NFAs and a rational molecular design strategy for creating new high-efficiency OSC materials *via* crystal engineering.

Conflicts of interest

There are no conflicts to declare.

Acknowledgements

A. K. Y. J. thanks the sponsorship of the Lee Shau-Kee Chair Professor (Materials Science), and the support from the APRC Grant of the City University of Hong Kong (9380086), Innovation and Technology Fund (ITS/497/18FP, GHP/021/18SZ), the US Office of Naval Research (N00014-20-1-2191), the GRF grant (11307621) and the CRF grant (C6023-19GF) from the Research Grants Council of Hong Kong, Guangdong Major Project of Basic and Applied Basic Research (2019B030302007), Guangdong-Hong Kong-Macao Joint Laboratory of Optoelectronic and Magnetic Functional Materials (2019B121205002). L. O. J., K. L. K., G. C. S. and T. J. M. acknowledge the support from the Center for Light Energy Activated Redox Processes (LEAP), an Energy Frontier Research Center funded by the U.S. Department of Energy, Office of Science, Office of Basic Energy Sciences, under Award #DE-SC0001059. T. J. M. acknowledges the US Office of Naval Research (N00014-20-1-2116). The authors also thank Dr Qunping Fan from the City University of Hong Kong and Dr Shanshan Chen from Chongqing University for their help in making this work more complete.

Notes and references

1 C. Yan, S. Barlow, Z. Wang, H. Yan, A. K.-Y. Jen, S. R. Marder and X. Zhan, *Nat. Rev. Mater.*, 2018, **3**, 18003–18021.
2 W. Xu and F. Gao, *Mater. Horiz.*, 2018, **5**, 206–221.
3 Y. Lin, J. Wang, Z. G. Zhang, H. Bai, Y. Li, D. Zhu and X. Zhan, *Adv. Mater.*, 2015, **27**, 1170–1174.
4 Q. Fan, H. Fu, Q. Wu, Z. Wu, F. Lin, Z. Zhu, J. Min, H. Y. Woo and A. K.-Y. Jen, *Angew. Chem., Int. Ed.*, 2021, **60**, 15935–15943.
5 F. Lin, L. Zuo, K. Gao, M. Zhang, S. B. Jo, F. Liu and A. K.-Y. Jen, *Chem. Mater.*, 2019, **31**, 6770–6778.
6 Y. Cui, H. Yao, J. Zhang, T. Zhang, Y. Wang, L. Hong, K. Xian, B. Xu, S. Zhang, J. Peng, Z. Wei, F. Gao and J. Hou, *Nat. Commun.*, 2019, **10**, 2515–2522.
7 F. Qi, Y. Zhang, M. Wan, J. Liu and L. Huo, *J. Mater. Chem. C*, 2018, **6**, 4208–4216.
8 L. Zhan, S. Li, X. Xia, Y. Li, X. Lu, L. Zuo, M. Shi and H. Chen, *Adv. Mater.*, 2021, **33**, 2007231.
9 Q. Liu, Y. Jiang, K. Jin, J. Qin, J. Xu, W. Li, J. Xiong, J. Liu, Z. Xiao, K. Sun, S. Yang, X. Zhang and L. Ding, *Sci. Bull.*, 2020, **65**, 272–275.
10 W. Gao, H. Fu, Y. Li, F. Lin, R. Sun, Z. Wu, X. Wu, C. Zhong, J. Min, J. Luo, H. Y. Woo, Z. Zhu and A. K.-Y. Jen, *Adv. Energy Mater.*, 2020, **11**, 2003177.
11 K. Jiang, Q. Wei, J. Y. L. Lai, Z. Peng, H. K. Kim, J. Yuan, L. Ye, H. Ade, Y. Zou and H. Yan, *Joule*, 2019, **3**, 3020–3033.
12 Y. Chang, T.-K. Lau, M.-A. Pan, X. Lu, H. Yan and C. Zhan, *Mater. Horiz.*, 2019, **6**, 2094–2102.
13 Z. Yao, X. Liao, K. Gao, F. Lin, X. Xu, X. Shi, L. Zuo, F. Liu, Y. Chen and A. K.-Y. Jen, *J. Am. Chem. Soc.*, 2018, **140**, 2054–2057.
14 H. Fu, W. Gao, Y. Li, F. Lin, X. Wu, J. H. Son, J. Luo, H. Y. Woo, Z. Zhu and A. K.-Y. Jen, *Small Methods*, 2020, **4**, 2000687.
15 W. Gao, B. Fan, F. Qi, F. Lin, R. Sun, X. Xia, J. Gao, C. Zhong, X. Lu, J. Min, F. Zhang, Z. Zhu, J. Luo and A. K.-Y. Jen, *Adv. Funct. Mater.*, 2021, **31**, 2104369.
16 S. Li, L. Zhan, Y. Jin, G. Zhou, T. K. Lau, R. Qin, M. Shi, C. Z. Li, H. Zhu, X. Lu, F. Zhang and H. Chen, *Adv. Mater.*, 2020, **32**, 2001160.
17 J. Yuan, Y. Zhang, L. Zhou, G. Zhang, H.-L. Yip, T.-K. Lau, X. Lu, C. Zhu, H. Peng, P. A. Johnson, M. Leclerc, Y. Cao, J. Ulanski, Y. Li and Y. Zou, *Joule*, 2019, **3**, 1140–1151.
18 H. Chen, H. Lai, Z. Chen, Y. Zhu, H. Wang, L. Han, Y. Zhang and F. He, *Angew. Chem., Int. Ed.*, 2020, **60**, 3238–3246.
19 L. Zhu, M. Zhang, G. Zhou, T. Hao, J. Xu, J. Wang, C. Qiu, N. Prine, J. Ali, W. Feng, X. Gu, Z. Ma, Z. Tang, H. Zhu, L. Ying, Y. Zhang and F. Liu, *Adv. Energy Mater.*, 2020, **10**, 1904234.
20 W. Zhu, A. P. Spencer, S. Mukherjee, J. M. Alzola, V. K. Sangwan, S. H. Amsterdam, S. M. Swick, L. O. Jones, M. C. Heiber, A. A. Herzing, G. Li, C. L. Stern, D. M. DeLongchamp, K. L. Kohlstedt, M. C. Hersam, G. C. Schatz, M. R. Wasielewski, L. X. Chen, A. Facchetti and T. J. Marks, *J. Am. Chem. Soc.*, 2020, **142**, 14532–14547.

21 X. Li, I. Angunawela, Y. Chang, J. Zhou, H. Huang, L. Zhong, A. Liebman-Peláez, C. Zhu, L. Meng, Z. Xie, H. Ade, H. Yan and Y. Li, *Energy Environ. Sci.*, 2020, **13**, 5028–5038.
22 G. Zhang, X.-K. Chen, J. Xiao, P. C. Y. Chow, M. Ren, G. Kupgan, X. Jiao, C. C. S. Chan, X. Du, R. Xia, Z. Chen, J. Yuan, Y. Zhang, S. Zhang, Y. Liu, Y. Zou, H. Yan, K. S. Wong, V. Coropceanu, N. Li, C. J. Brabec, J.-L. Bredas, H.-L. Yip and Y. Cao, *Nat. Commun.*, 2020, **11**, 3943–3952.
23 F. Lin, K. Jiang, W. Kaminsky, Z. Zhu and A. K.-Y. Jen, *J. Am. Chem. Soc.*, 2020, **142**, 15246–15251.
24 J. Yuan, T. Huang, P. Cheng, Y. Zou, H. Zhang, J. L. Yang, S. Y. Chang, Z. Zhang, W. Huang, R. Wang, D. Meng, F. Gao and Y. Yang, *Nat. Commun.*, 2019, **10**, 570–577.
25 R. Wang, J. Yuan, R. Wang, G. Han, T. Huang, W. Huang, J. Xue, H. C. Wang, C. Zhang, C. Zhu, P. Cheng, D. Meng, Y. Yi, K. H. Wei, Y. Zou and Y. Yang, *Adv. Mater.*, 2019, **31**, 1904215.
26 C. Zhu, J. Yuan, F. cai, L. Meng, H. Zhang, H. Chen, J. Li, B. Qiu, H. Peng, S. Chen, Y. Hu, C. Yang, F. Gao, Y. Zou and Y. Li, *Energy Environ. Sci.*, 2020, **13**, 2459–2466.
27 S. Liu, J. Yuan, W. Deng, M. Luo, Y. Xie, Q. Liang, Y. Zou, Z. He, H. Wu and Y. Cao, *Nat. Photonics*, 2020, **14**, 300–305.
28 F. Qi, K. Jiang, F. Lin, Z. Wu, H. Zhang, W. Gao, Y. Li, Z. Cai, H. Y. Woo, Z. Zhu and A. K.-Y. Jen, *ACS Energy Lett.*, 2021, **6**, 9–15.
29 Y. Cui, H. Yao, J. Zhang, K. Xian, T. Zhang, L. Hong, Y. Wang, Y. Xu, K. Ma, C. An, C. He, Z. Wei, F. Gao and J. Hou, *Adv. Mater.*, 2020, **32**, 1908205.
30 G. Chai, Y. Chang, J. Zhang, X. Xu, L. Yu, X. Zou, X. Li, Y. Chen, S. Luo, B. Liu, F. Bai, Z. Luo, H. Yu, J. Liang, T. Liu, K. S. Wong, H. Zhou, Q. Peng and H. Yan, *Energy Environ. Sci.*, 2021, **14**, 3469–3479.
31 T. Liu, L. Huo, S. Chandrabose, K. Chen, G. Han, F. Qi, X. Meng, D. Xie, W. Ma, Y. Yi, J. M. Hodgkiss, F. Liu, J. Wang, C. Yang and Y. Sun, *Adv. Mater.*, 2018, **30**, 1707353.
32 L. Huo, X. Xue, T. Liu, W. Xiong, F. Qi, B. Fan, D. Xie, F. Liu, C. Yang and Y. Sun, *Chem. Mater.*, 2018, **30**, 3294–3300.
33 I. Meager, R. S. Ashraf, S. Mollinger, B. C. Schroeder, H. Bronstein, D. Beatrup, M. S. Vezie, T. Kirchartz, A. Salleo, J. Nelson and I. McCulloch, *J. Am. Chem. Soc.*, 2013, **135**, 11537–11540.
34 C. Li, J. Zhou, J. Song, J. Xu, H. Zhang, X. Zhang, J. Guo, L. Zhu, D. Wei, G. Han, J. Min, Y. Zhang, Z. Xie, Y. Yi, H. Yan, F. Gao, F. Liu and Y. Sun, *Nat. Energy*, 2021, **6**, 605–613.
35 R. C. Coffin, J. Peet, J. Rogers and G. C. Bazan, *Nat. Chem.*, 2009, **1**, 657–661.
36 Y. Tsutsui, G. Schweicher, B. Chattopadhyay, T. Sakurai, J. B. Arlin, C. Ruzie, A. Aliev, A. Ciesielski, S. Colella, A. R. Kennedy, V. Lemaur, Y. Olivier, R. Hadji, L. Sanguinet, F. Castet, S. Osella, D. Dudenko, D. Beljonne, J. Cornil, P. Samori, S. Seki and Y. H. Geerts, *Adv. Mater.*, 2016, **28**, 7106–7114.
37 T. J. Aldrich, M. Matta, W. Zhu, S. M. Swick, C. L. Stern, G. C. Schatz, A. Facchetti, F. S. Melkonyan and T. J. Marks, *J. Am. Chem. Soc.*, 2019, **141**, 3274–3287.
38 S. M. Swick, T. Gebraad, L. Jones, B. Fu, T. J. Aldrich, K. L. Kohlstedt, G. C. Schatz, A. Facchetti and T. J. Marks, *ChemPhysChem*, 2019, **20**, 2608–2626.
39 H. Huang, L. Yang, A. Facchetti and T. J. Marks, *Chem. Rev.*, 2017, **117**, 10291–10318.
40 N. E. Jackson, B. M. Savoie, K. L. Kohlstedt, M. Olvera de la Cruz, G. C. Schatz, L. X. Chen and M. A. Ratner, *J. Am. Chem. Soc.*, 2013, **135**, 10475–10483.
41 W. Yan, T. Liao, O. Tuguldur, C. Zhong, J. L. Petersen and X. Shi, *Chem. – Asian J.*, 2011, **6**, 2720–2724.
42 M. Más-Montoya and R. A. J. Janssen, *Adv. Funct. Mater.*, 2017, **27**, 1605779.
43 N. J. Hestand and F. C. Spano, *Chem. Rev.*, 2018, **118**, 7069–7163.
44 G. Li, X. Zhang, L. O. Jones, J. M. Alzola, S. Mukherjee, L. W. Feng, W. Zhu, C. L. Stern, W. Huang, J. Yu, V. K. Sangwan, D. M. DeLongchamp, K. L. Kohlstedt, M. R. Wasielewski, M. C. Hersam, G. C. Schatz, A. Facchetti and T. J. Marks, *J. Am. Chem. Soc.*, 2021, **143**, 6123–6139.
45 S. M. Swick, J. M. Alzola, V. K. Sangwan, S. H. Amsterdam, W. Zhu, L. O. Jones, N. Powers-Riggs, A. Facchetti, K. L. Kohlstedt, G. C. Schatz, M. C. Hersam, M. R. Wasielewski and T. J. Marks, *Adv. Energy Mater.*, 2020, **10**, 2000635.
46 R. Wang, C. Zhang, Q. Li, Z. Zhang, X. Wang and M. Xiao, *J. Am. Chem. Soc.*, 2020, **142**, 12751–12759.
47 J. Benduhn, K. Tvingstedt, F. Piersimoni, S. Ullbrich, Y. Fan, M. Tropiano, K. A. McGarry, O. Zeika, M. K. Riede, C. J. Douglas, S. Barlow, S. R. Marder, D. Neher, D. Spoltore and K. Vandewal, *Nat. Energy*, 2017, **2**, 17053–17058.
48 Q. Fan, R. Ma, T. Liu, J. Yu, Y. Xiao, W. Su, G. Cai, Y. Li, W. Peng, T. Guo, Z. Luo, H. Sun, L. Hou, W. Zhu, X. Lu, F. Gao, E. Moons, D. Yu, H. Yan and E. Wang, *Sci. China: Chem.*, 2021, **64**, 1380–1388.
49 H. Xu, Y. Yang, C. Zhong, X. Zhan and X. Chen, *J. Mater. Chem. A*, 2018, **6**, 6393–6401.
50 W. Gao, M. Zhang, T. Liu, R. Ming, Q. An, K. Wu, D. Xie, Z. Luo, C. Zhong, F. Liu, F. Zhang, H. Yan and C. Yang, *Adv. Mater.*, 2018, **30**, 1800052.

